Multichannel Staggered SAR Azimuth Sample Regularization

Felipe Queiroz de Almeida, Gerhard Krieger
German Aerospace Center (DLR), Microwaves and Radar Institute, felipe.queirozdealmeida@dlr.de
Wessling, Germany

Abstract

Next-generation spaceborne SAR systems pose demanding and contradicting requirements on system design, owing to the increasing need to cover ultra-wide swaths with high azimuth resolution, as required for numerous applications. To this end, a large number of multichannel SAR system concepts have been proposed that employ digital beamforming on receive with planar arrays, and more recently also with reflector antennas. A promising concept is *staggered SAR* which uses a single azimuth channel and multiple elevation beams together with variable pulse repetition intervals to map an arbitrary wide swath with medium resolution. To improve the azimuth resolution, this paper extends the staggered SAR concept to a system configuration with multiple azimuth channels. For this, a new multichannel azimuth processing technique is introduced that combines staggered SAR gap interpolation with multi-channel SAR signal reconstruction. Simulations of a Tandem-L-like reflector SAR system with three azimuth channels show that this technique yields an excellent performance over a 350 km wide swath that is mapped with 3.0 m azimuth resolution.

1 Introduction

Next-generation spaceborne SAR imaging systems, such as DLR's Tandem-L mission proposal [1], require a short revisit time coupled with high resolution to enable a global and systematic observation of Earth dynamic processes, which are the object of various scientific and environmental studies. Wide swath coverage and high azimuth resolution pose, however, contradicting requirements on SAR system design. To solve this contradiction, and to outperform current state-of-the-art systems, next-generation SAR systems will employ new digital beamforming techniques [2].

Multichannel SAR systems with digital beamforming in azimuth [3], [4] have been proposed as a possible solution for coping with these challenging requirements and achieving high-resolution wide swath (HRWS) imaging capabilities, initially in planar array antenna systems and more recently also in conjunction with reflector-based antennas [5]. *Staggered SAR* [6] has been proposed as an alternative to increase the swath width of SAR systems with a single azimuth channel. The technique employs digital beamforming in elevation to implement multiple simultaneous beams, and relies on a varying pulse repetition interval (PRI) to avoid *blind ranges*, caused by the impossibility to record the received signal while simultaneously transmitting, over the swath. The reader is referred to [6], [7] for details of the technique and design procedures for the PRIs.

This paper combines the staggered SAR technique with multichannel system architectures in azimuth, thus introducing new and potentially highly flexible modes of operation. Moreover, a new processing technique is introduced that enables the mapping of ultra-wide swaths with very high azimuth resolution and excellent ambiguity performance. The paper provides therefore an important contribution to the new developments in the field of digital beamforming techniques for next-generation spaceborne SAR missions.

2 The Multichannel Staggered-PRI Sample Regularization Problem

2.1 Problem Description

The received azimuth signal of a staggered SAR is sampled in a periodically non-uniform manner and is subject to range-dependent gaps induced by blockage of the received pulses, whenever pulse transmission occurs. Furthermore, a system with multiple azimuth channels is assumed, capable of recording N_{ch} samples per received pulse. In order to apply conventional SAR processing to such a signal, one is interested in obtaining from the effective N_{eff} staggered PRI pulses a regularly sampled output at an increased rate of $PRF_{multi} = N_{ch} \cdot \overline{PRF}_{eff}$, where $\overline{PRF}_{eff}$ is the effective average sampling rate of the pulses, accounting for blockage. The desired resampling operation is represented schematically for a cycle of pulses in **Figure 1**. Out of the N_{PRI} transmitted pulses in a cycle, $N_{eff} \leq N_{PRI}$ are effectively received, yielding N_{ch} samples each. The goal is to combine in time domain all the available samples over all channels and pulses in the cycle to recover a uniformly sampled SAR signal composed of $N = N_{eff} \cdot N_{ch}$ samples per cycle.

ISBN 978-3-8007-4228-8 / ISSN 2197-4403

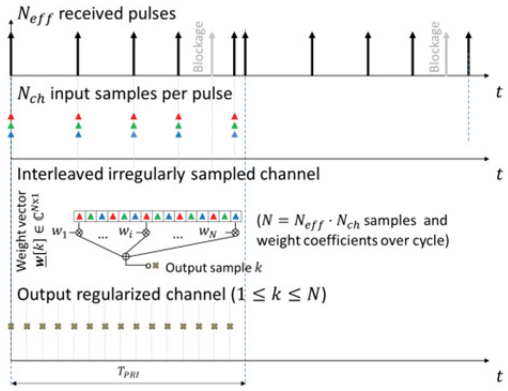

Figure 1: Required resampling operation over a cycle of pulses of duration T_{PRI}.

This may be achieved by a linear combination of the N input samples, where the weights depend on the output sample position k. As elaborated in the next section, the corresponding weight vector $\underline{\boldsymbol{w}}[k]$ is designed to achieve a suitable phase relation of the output patterns that characterize each sample in the output grid.

2.2 Optimal Mean Squared Error Solution

Acquisition of the azimuth signal through multiple phase centers [3] is the key to the uniform signal reconstruction capability. For instance, *uniform array steering* [8], [9] with the feed beam may be employed to obtain patterns with different phase centers which still observe the same Doppler spectrum on ground. This is achieved by illuminating different regions of the reflector's surface. Illuminating a subset instead of the whole of the reflector broadens the resulting patterns on ground. Nonetheless, the ability to continuously vary the primary beam's position allows adjustment of the phase centers to achieve the needed sample regularization.

Based on *least-squares (LS) pattern synthesis* [10], a method is proposed which builds on this concept, further exploiting the interchangeability between the pattern's phase center and the corresponding sample position. The original LS pattern synthesis problem may be described as follows. Given an arbitrary N-element array manifold vector [10]

$$\underline{\boldsymbol{v}}(f_d) = [v_1(f_d) \quad \dots \quad v_N(f_d)]^T, \tag{1}$$

which collects the N complex antenna patterns $v_i(f_d)$ as a function of the Doppler frequency f_d, derive the beamforming weight vector $\underline{\boldsymbol{w}}$ that leads to the closest approximation $\hat{G}_{GOAL}(f_d) = \underline{\boldsymbol{w}}^{\boldsymbol{H}} \cdot \underline{\boldsymbol{v}}(f_d)$ of a desired pattern $G_{GOAL}(f_d)$. The solution is achieved by minimizing a cost function that measures the integral of the mean squared error (MSE) between the goal pattern and the approximation, i.e.,

$$\xi_{MSE} = \int \left(G_{GOAL}(f_d) - \underline{\boldsymbol{w}}^{\boldsymbol{H}} \cdot \underline{\boldsymbol{v}}(f_d)\right)^2 df_d, \tag{2}$$

where the region of integration has to be appropriately chosen, for instance PRF_{multi}. A Doppler-frequency dependent weighting of the integral may also be applied.

In the following, this technique will be applied to the resampling problem at hand by accounting also for the different sampling positions. Though only N_{ch} physical channels exist, an extended array manifold vector of length $N = N_{eff} \cdot N_{ch}$ can be considered for the system, augmenting the manifold vector of the physical channels with a phase ramp describing the pulse position in the sampling over the cycle. For this, we denote the time instants of the received pulses, which may be obtained by timing analysis of the PRI sequence [6], [7], by $t_{RX}[i]$, $1 \le i \le N_{eff}$, and the complex patterns of the N_{ch} azimuth channels by $G_n(f_d)$, $1 \le n \le N_{ch}$. The elements of the extended manifold, which models the input samples over all $N_{eff} \cdot N_{ch}$ channels, can then be written as

$$\boldsymbol{v}_k(f_d) = G_{k_1[k]}(f_d) \cdot \exp(-j \cdot 2 \cdot \pi \cdot t_{RX}[k_2[k]] \cdot f_d), \tag{3}$$

$1 \le k \le N$. As k varies, the pattern indices $k_1[k]$ vary cyclically from 1 to N_{ch}, and the sample indices $k_2[k]$ repeat themselves N_{ch} times before being incremented by one. This ensures that all azimuth channels for a given pulse position are taken as part of the manifold. The indices k_1 and k_2 can be expressed mathematically as $k_1[k] = 1 + (k \bmod N_{ch})$, with mod denoting the modulo (integer division remainder) operator, and $k_2[k] = k \,\%\, N_{ch}$, with % denoting the quotient of integer division.

The desired output samples form a regular grid at the increased sampling rate of N samples per cycle. This can be described by a set of N output patterns $G_{GOAL}(f_d, k)$, one for each sample $1 \le k \le N$, with phase relations implied by

$$G_{GOAL}(f_d, k) = G_{common}(f_d) \cdot \exp(-j \cdot 2 \cdot \pi \cdot t_{out}[k] \cdot f_d), \tag{4}$$

where $G_{common}(f_d)$ is a common pattern for all output channels and

$$t_{out}[k] = \frac{k-1}{N_{ch} \cdot \overline{PRF}_{eff}} + \delta t, \tag{5}$$

denotes the sampling instants of the output grid, regular by definition. The parameter δt is an arbitrary time shift which doesn't change the regularity property of the grid and can be used as a degree of freedom in the design. Minimizing the maximum required sample position shift is a reasonable criterion for its choice.

The desired output patterns in (4) should, up to the linear phase ramp, be similar to the patterns expected in the

case of *uniform array steering* [9], although the number of elements in the manifold differs. In that case, the phase relations are determined by the scan angle to which the feed pattern is steered to, and the resulting illuminated area on the reflector. Meanwhile, $G_{common}(f_d)$ is under certain conditions equal to the *sum pattern* of all physical channels

$$G_{sum}(f_d) = \frac{1}{N_{ch}} \cdot \sum_{i=1}^{N_{ch}} G_i(f_d), \tag{6}$$

which in the case of reflectors is broader and illuminates approximately the combined beam width of the elements. The sum pattern of the physical channels remains a reasonable choice for the design of $G_{common}(f_d)$ in (8), though this degree of freedom may also be exploited (cf. Section 2.4). It should be noted that the proposed modeling of each sample by means of an equivalent pattern through (3) and (4) effectively transforms the initial resampling problem of Section 2.1 into a more tractable pattern synthesis problem.

The solution to the optimum weights in the MSE sense can be obtained by minimizing (2) by means of its complex gradient [10]. This leads, for each k, to a solution proportional to the cross-correlation between the goal pattern and the array manifold vector,

$$\underline{\boldsymbol{\sigma}}_{\boldsymbol{G}} \triangleq \int G^*_{GOAL}(f_d) \cdot \underline{v}(f_d)\, df_d \tag{7}$$

weighted by the inverse of the array manifold's cross-correlation matrix

$$\underline{\boldsymbol{R}}_{\boldsymbol{v}} \triangleq \int \underline{\boldsymbol{v}}(f_d) \cdot \underline{\boldsymbol{v}}(f_d)^H\, df_d. \tag{8}$$

The optimum MSE weights are then given by

$$\underline{\boldsymbol{w}}_{MSE} = \underline{\boldsymbol{R}}_{\boldsymbol{v}}^{-\mathbf{1}} \cdot \underline{\boldsymbol{\sigma}}_{G}. \tag{9}$$

This solution has the desirable property of achieving the closest possible implementation of the desired set of output patterns.

The structure of (9) implies that the method automatically selects – from the physical channels in different positions during the pulse cycles – the elements which are more correlated to a particular output position. Even though the baselines introduce, as expected, a notable decorrelation between the elements of the proposed extended manifold, no degradation ensues from the use of additional channels. Should they be too distant from the desired sample position and thus uncorrelated, the corresponding weights are accordingly very low in magnitude. The small gain avoids therefore a possible degradation from uncorrelated samples.

2.3 Extension to Accommodate Noise Rejection: Joint Cost Function

It should nonetheless be noted that the use of several potentially poorly correlated channels may lead to a beamformer with poor signal to noise ratio (SNR) gain in comparison to other alternatives, especially when obtaining samples within the gaps. To counter this, a normalized SNR measurement [10] with respect to white noise

$$\xi_{SNR} = \frac{\underline{\boldsymbol{w}}^H \cdot \underline{\boldsymbol{R}}_{\boldsymbol{v}} \cdot \underline{\boldsymbol{w}}}{\underline{\boldsymbol{w}}^H \cdot \underline{\boldsymbol{w}}}, \tag{10}$$

may be incorporated into the cost function, leading to a joint MSE-SNR cost function of the form

$$\xi_J = (1-\alpha) \cdot \frac{\xi_{MSE}}{n_{MSE}} + \alpha \cdot \frac{n_{SNR}}{\xi_{SNR}}, \tag{11}$$

where n_{MSE} and n_{SNR} are normalization factors, which allow the MSE and SNR to be matched in terms of numerical values, and α is a design parameter. $\alpha = 0$ leads to the optimal MSE solution, while increasing values up to $\alpha = 1$, a limiting case that disregards the goal pattern completely, emphasizes the SNR of the solution. Clearly the normalization factors play also a role in the sensitivity of the cost function to the design parameter α. A similar strategy is adopted in [4], though in a different optimization context.

Applying the complex gradient to (11) leads to a nonlinear system of equations to determine the N optimal complex weights, which nonetheless may be solved numerically using the closed form solutions available for the limiting cases $\alpha = 0$ or $\alpha = 1$ as first guesses.

A possible figure of merit for the SNR of the pattern achieved by means of arbitrary weights $\underline{\boldsymbol{w}}$ is given by the integral of the patterns' gain inside the processed bandwidth Bw_{proc}, normalized by the same integral for a reference pattern. This reference is here chosen to be $G_{sum}(f_d)$, yielding the quantity

$$\Phi_{SNR}(\underline{\boldsymbol{w}}) = \frac{1}{k_{sum}} \cdot \frac{1}{\underline{\boldsymbol{w}}^H \cdot \underline{\boldsymbol{w}}} \cdot \int_{Bw_{proc}} \left|\underline{\boldsymbol{w}}^{\boldsymbol{H}} \cdot \underline{\boldsymbol{v}}(f_d)\right|^2 df_d, \tag{12}$$

where the normalization factor is given by

$$k_{sum} = \frac{1}{N_{ch}} \cdot \int_{Bw_{proc}} \left| \sum_{i=1}^{N_{ch}} G_i(f_d) \right|^2 df_d. \tag{13}$$

2.4 Extension to Accommodate Pattern Distortions: Iterative Synthesis

Regardless of whether (2) or (11) are minimized, the optimization takes place using information from a single output sample at a time. Furthermore, residual distortions will occur as a rule, as the implemented patterns are imperfect approximations of the goals. As the procedure is repeated over all samples to form the output grid, owing to the irregularity of $t_{RX}[i]$, some pattern approximations are less successful than others. This is especially true for the output samples that span the blockage-induced gaps, as there larger shifts of the

phase centers with respect to the inputs are required. It is thus desirable to use information from other output samples in the grid to implement a given pattern $G_{GOAL}(f_d, k)$, in order to better equalize the performance over the samples.

A simple way of doing this is to exploit the degree of freedom $G_{common}(f_d)$ in (4). As long as the phase relations regarding $t_{out}[k]$ hold, the output grid remains regular, and enforcing $G_{common}(f_d) = G_{sum}(f_d)$ is not strictly necessary. The common pattern can also be shaped such that the output grid is more readily implementable by the given input manifold. The incorporation of an average distortion to the common component of the design goals may lead to more readily achievable patterns without violating the regularity, the main objective of the resampling. Moreover, if the design is done iteratively, the information from the other patterns in the grid is readily available at the end of each iteration. One may thus propose the following logic for the common pattern design. The previous choice is maintained for the first iteration, i.e.,

$$G^0_{common}(f_d) = G_{sum}(f_d). \tag{14}$$

However, at iteration i,

$$G^{i+1}_{common}(f_d) = \frac{1}{N} \cdot \sum_{k=1}^{N} (\underline{\boldsymbol{w}}^{\boldsymbol{i}}\ [k])^{\boldsymbol{H}} \cdot \underline{\boldsymbol{v}}(f_d) \cdot \exp(+j \cdot 2 \cdot \pi \cdot t_{out}[k] \cdot f_d\ ), \tag{15}$$

where $\underline{\boldsymbol{w}}^{\boldsymbol{i}}\ [k]$ denotes the weights for the k^{th} pattern in the grid. This means that the mean common pattern achieved by the implementation is calculated, and passed on as a less strict design goal to the next iteration. This allows lower MSEs to be achieved in the worst cases over the grid and thus improves the overall approximation. It should be noted that, if (2) is used, lower MSEs than those of the method in Section 2.2 may be obtained because of the change in the design goal, hence without contradiction to the optimality of that method. A degradation of $G_{common}(f_d)$ in comparison to the initial sum pattern is possible, but the impact is small as long as the worst-case distortions are not excessive. The effect can be controlled by proper design of the PRI sequence.

A stop criterion for the iteration is needed, and one possibility is the step in the average MSE over the grid from the current iteration to the last. If (11) is used, it is also possible to use an average of the SNR figure of (12). In the latter case, a feedback of the parameter α into the design goal tends to enhance the emphasis on the SNR and improve the performance with this regard, though increasing the minimum achievable MSE and possibly slowing convergence to lower MSE values.

3 Simulation Results and Analysis

In the following, the performance of the different methods will be analyzed and compared, taking as reference one of the high azimuth resolution modes of the Tandem-L mission proposal [1]. The goal is to image from an orbit height of 745 km a swath of 350 km on ground with 3.0 m azimuth resolution in L-band, using a parabolic reflector antenna architecture [5], as illustrated in **Figure 2**.

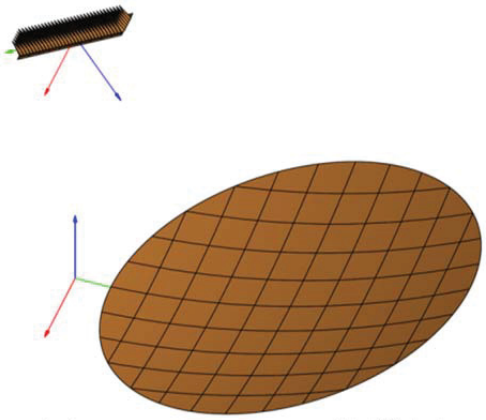

Figure 2: Antenna system geometry highlighting multichannel feed and reflector rim. The feed system consists of 32 elements in elevation and 6 in azimuth, combined pairwise to form 3 channels.

As a first example, a simulated point target in the center of the scene at a ground range of 485 km is considered. The non-uniformly sampled multichannel signal is resampled by the aforementioned methods and then focused in azimuth by conventional SAR processing, yielding corresponding impulse responses. The relevant system parameters are summarized in **Table 1**.

Platform and swath parameters	
Parameter	Value
Orbit height h_{orbit}	745 km
Swath width on ground	350 km
Swath minimum/maximum slant range	821 km /1033 km
Reflector and feed parameters	
Parameter	Value
Diameter	15.0 m
Focal length	7.5 m
Feed offset in elevation	9.0 m
Center frequency	1.2575 GHz
Number of channels in elevation/azimuth	32 / 3
Channel spacing in elevation/azimuth	0.68 λ / 1.2 λ
Elevation tilt angle	32.4 deg
Pulse parameters	
Parameter	Value
Average PRF $\overline{PRF}$	2700 Hz
Initial PRI PRI_0	386 µs
PRI sequence step Δ	-0.98 µs
PRI sequence length N_{PRI}	33
Pulse length T_p	14.8 µs
Processing parameters	
Parameter	Value
Processed bandwidth Bw_{proc}	2494 Hz

Table 1: Relevant system parameters.

Blockage analysis [6], [7] shows for this case that from the sequence of $N_{PRI} = 33$ pulses, the 3rd and the 32nd are lost due to blockage, leading to an effective number of pulses $N_{eff} = 31$, and the sampling configuration represented in **Figure 3**.

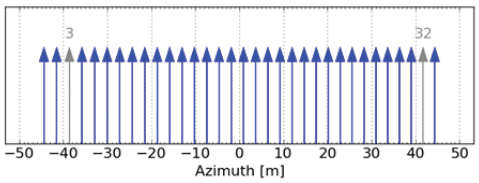

Figure 3: Azimuth sampling and blocked pulses (in grey) over one PRI sequence cycle at a ground range of 485 km.

The output regular grid has $N = 93$ samples over a PRI cycle. Evaluating the optimal MSE weights for every sample using (4) and (5) leads to the 93 patterns depicted in **Figure 4**.

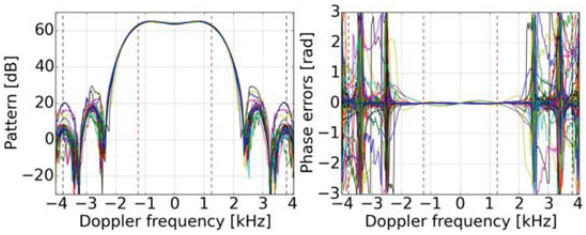

Figure 4: Set of output patterns obtained from the optimal MSE method: magnitude (left) and phase after removal of the sample-specific linear phase ramp (right), indicating residual phase errors with respect to ideal regular sampling. Bw_{proc} is marked by red dashed lines.

Within the main beam, the patterns show stable magnitudes and very low residual phase errors with respect to the desired baselines, which indicates successful regularization. The MSE – normalized to the power of the *sum pattern* – and the SNR scaling Φ_{SNR} of (12) over the output patterns are shown for different methods in **Figure 5**. The plots on the top refer to the optimum MSE method of Section 2.2. The ones in the middle were obtained with the method of Section 2.3, evaluated with $\alpha = 0.6$. The plots on the bottom show the results for the iterative method of Section 2.4, again using (11) with $\alpha = 0.6$.

A comparison of the results on the top and in the middle of **Figure 5** highlights the compromise between MSE and SNR, embodied by the design parameter α. Introducing the iterative procedure (middle vs. bottom) enhances on average both figures, with a larger improvement for the worst cases. The ripple in Φ_{SNR} over the samples is also reduced. In all cases, the performance for the samples within the region of the blockage-induced gaps is clearly worse. This is expected and due to the larger phase center shift with respect to the input grid required to fill those gaps.

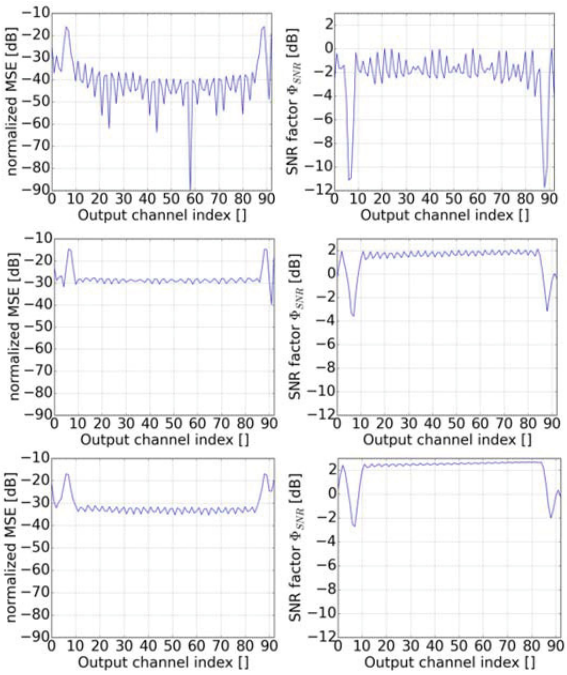

Figure 5: Normalized MSE and Φ_{SNR} over output patterns/samples for optimum MSE (top), non-iterative joint MSE-SNR (middle) and iterative joint MSE-SNR (bottom) LS regularization methods. For the last two methods, $\alpha = 0.6$.

The focused impulse responses (IRs) of the data regularized by the first two methods are depicted in **Figure 6**, plotted against the instantaneous Doppler. The IR for the third method is not shown due to its similarity to the other plots. The several azimuth ambiguities seen in the impulse responses of the regularized data occur at multiples of $\overline{PRF}_{eff}$ / N_{eff}, as a result of residual regularization errors (cf. **Figure 4**). Their peak level is nonetheless very low, indicating successful application of the methods for resampling. It should be noted that $\overline{PRF}_{eff}$ / N_{eff} = 1 / T_{PRI} is the rate at which the PRI sequence repeats itself, and that the residual deviations between the achieved patterns and the ideal $G_{GOAL}(f_d, k)$ lead to a periodical modulation of the samples in the output channel at this rate.

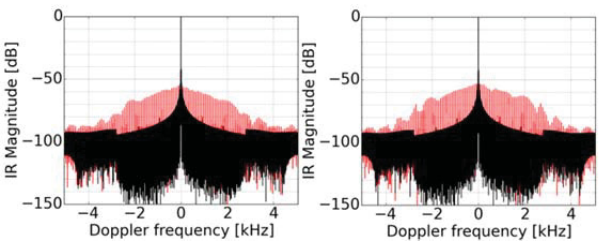

Figure 6: Impulse responses of regularized data (red) and alias-free reference regularly sampled at PRF_{multi} (black), for the optimal MSE method [10] (left) and joint MSE-SNR method (right).

Figures of merit for the regularizations' output patterns and the impulse responses are summarized in **Table 2**. There, δ_{AZ} is the 3dB azimuth resolution, AA_{PEAK} and AASR describe respectively peak and total azimuth ambiguity levels, while $\overline{MSE}$ and $\overline{\Phi_{SNR}}$ are averages (taken in linear units and then converted to dB) of the quantities in **Figure 5**. Estimation of AASR in staggered SAR is addressed in [11] in detail.

Figure of merit	Optimal MSE-LS	Joint MSE-SNR LS	Iterative Joint MSE-SNR LS
δ_{AZ} [m]	2.4	2.4	2.4
AA_{PEAK} [dB]	-55.3	-53.1	-53.3
AASR [dB]	-40.2	-37.3	-36.8
$\overline{MSE}$ [dB]	-28.9	-25.4	-27.6
$\overline{\Phi_{SNR}}$ [dB]	-1.9	1.4	2.2

Table 2: Achieved pattern and impulse response figure of merit comparison between LS methods.

The resolution goal of 3.0 m is achieved and acceptably low AASR levels are obtained for all methods. Furthermore, the proposed joint optimization is seen to allow a considerable gain in SNR at the expense of an acceptably small loss in MSE and AASR levels. Since the design goal of (4) is to enforce regularity, the MSE and AASR levels are directly linked. It should, however, be noted that $G_{common}(f_d)$ also affects the final MSE levels, and the change in this parameter between the two last methods is the reason why the iterative method achieved a slightly worse AASR despite better $\overline{MSE}$.

As a reference, Φ_{SNR} for a frequency-adaptive MVDR beam [5] yields 3.2 dB. This technique requires Doppler-dependent weights and cannot directly be implemented without a regularly sampled input, but may be employed as an SNR upper bound. The proximity of the levels indicates that the performance achieved by means of the joint optimization is also satisfactory with regard to noise rejection.

A limitation of the current formulation of the methods is namely that only the pulses within a cycle of PRIs are taken as part of the array manifold, and consequently the input grid. No such limitation occurs in practice, and samples from other cycles may also be employed to recover the output grid. The modeling of the manifold can thus be extended to allow for an overlap, e.g. half a cycle of PRIs, between cycles. This impacts mostly the samples in the beginning and the end of a cycle, but also contributes to reduce the maximum phase center shifts required for resampling and improves performance in general. A gain is expected especially for ranges in which the blocked pulses are at the cycle borders. In **Figure 7**, the joint iterative method with $\alpha = 0.6$ was applied to all ranges in the swath, considering the overlap extension. AASR levels (left) are below -30 dB. Performance is worst at near and far ranges due to antenna pattern defocusing. The extremely low levels at certain intervals (e.g. 400-420 km) occur when no pulses in the PRI sequence are blocked. $\overline{\Phi_{SNR}}$ is better than 1.8 dB and δ_{AZ} better than 3.0 m over the whole swath. It should be noted that the calculation of RASR (right) for staggered SAR requires some special considerations [11]. The levels are lower than -27 dB over the swath.

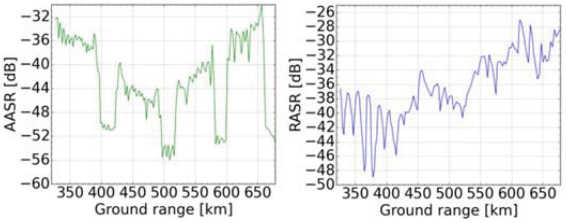

Figure 7: AASR (left) and RASR (right) performance over ground range for 350 km swath.

References

[1] A. Moreira et al.: *Tandem-L: A Highly Innovative Bistatic SAR Mission for Global Observation of Dynamic Processes on the Earth's Surface* IEEE Geoscience and Remote Sensing Magazine, Vol. 3, No. 2, pp.8-23, 2015.

[2] G. Krieger et al.: *Advanced Concepts for Ultra-Wide-Swath SAR Imaging* Proceedings of European Conference of Synthetic Aperture Radar (EUSAR), Vol. 1, pp.1-4, 2008.

[3] N. Gebert, G. Krieger, A. Moreira: *Digital Beamforming on Receive: Techniques and Optimization Strategies for High-Resolution Wide-Swath SAR Imaging* IEEE Transactions on Aerospace and Electronic Systems, Vol. 45, No. 2, pp.564-592, 2009.

[4] I. Sikaneta, C. H. Gierull and D. Cerutti-Maori: *Optimum Signal Processing for Multichannel SAR: With Application to High-Resolution Wide-Swath Imaging* IEEE Transactions on Geoscience and Remote Sensing, Vol. 52, No. 10, pp. 6095-6109, 2014.

[5] S. Huber, A. Patyuchenko, G. Krieger, A. Moreira: *Spaceborne Reflector SAR Systems with Digital Beamforming* IEEE Transactions on Aerospace and Electronic Systems, Vol. 48, No. 4, pp.3473-3493, 2012.

[6] M. Villano, G. Krieger, A. Moreira: *Staggered SAR: High-Resolution Wide-Swath Imaging by Continuous PRI Variation* IEEE Transactions on Geoscience and Remote Sensing, Vol. 52, no.7, pp.4462-4479, 2014.

[7] M. Villano, G. Krieger, A. Moreira: *A Novel Processing Strategy for Staggered SAR* IEEE Geoscience and Remote Sensing Letters, Vol. 11, No. 11, pp.1891-1895, 2014

[8] C. Balanis: *Antenna Theory: Analysis and Design*, John Wiley & Sons Inc., 1997.

[9] S. Bertl, P. Lopez-Dekker, M. Younis, G. Krieger: *Along-track SAR interferometry using a single reflector antenna*, IET Radar Sonar & Navigation, Vol. 9, No. 8, pp. 942 – 947, October 2015.

[10] H. L. V. Trees: *Optimum Array Processing*, John Wiley & Sons Inc., 2002.

[11] M. Villano, G. Krieger and A. Moreira: *Ambiguities and image quality in staggered SAR* Asia-Pacific Conference on Synthetic Aperture Radar (APSAR), pp. 204-209, 2015.